Not THE title: Plume velocity determination: comparison of methods

Arve Kylling[1], Jonas Gliss[2], Hamidreza Ardeshiri[1], Massimo Cassiani[1], Anna Solvejg Dinger[3], Soon-Young Park[4], Ignacio Pisso[1], Norbert Schmidbauer[1], Kerstin Stebel[1], and Andreas Stohl[1]

[1]NILU - Norwegian Institute for Air Research, NO-2007 Kjeller, Norway
[2]Norwegian Meteorological Institute, Oslo, Norway
[3]PGS, Oslo, Norway
[4]Center for Earth and Environmental Modeling Studies, Gwangju Institute of Science and Technology, Gwangju, Republic of Korea

Correspondence to: Arve Kylling (arve.kylling@nilu.no)

Abstract. To come

Things that could be interesting to vary in simulations are:

5
- Have a little older plume so that the range of detectable AA values covers a little more pixels in the vertical (maybe Hamid et al need to increase the emissions in that case, so that we get enough AA in the older plume).

-

- background wind velocity (e.g. between 1 and 10 m/s)

- background wind direction (e.g. simulate plume / camera CFOV angle range of e.g. 70 to 110 degrees)

10
- turbulent intensity (i.e. spectrum of velocity vector magnitudes and orientations -> could be interesting to see how the smoothness constraint of optical flow algorithms impacts the pixel based velocity estimates).

- It could be also interesting to see a convective version of the plume at very low velocities and investigate if the optical flow can capture the decrease in velocity between the centre and the edges of the plume.

- Also, if we have a higher signal in the aged plume (i.e. AA of the order of 0.1-1.0), then the very young plume probably

15
suffers saturation and hence shows little contrast for the velocity retrieval. Could be interesting to see how this impacts the optical flow velocities too.

1 Introduction

Describe earlier work

Describe what is done in this paper

20 The paper ends with the conclusions in section 4.

2 Methods

The large eddy and the radiative transfer simulations have been described in detail by Kylling et al. (2020) and are briefly summarized here for completeness.

2.1 Large eddy simulation (LES)

25 In LES the large scales of the turbulent flow are explicitly simulated while a low-pass filter is applied to the governing equations to remove the small scales information from the numerical solution. The effects of the small scales are then parameterized by means of a sub-grid scale (SGS) model (e.g. Deardorff, 1973; Moeng, 1984; Pope, 2000; Celik et al., 2009). We calculated the

3D SO$_2$ concentrations as a function of time in a three dimensional domain of 1000 m × 375 m × 250 m in the along wind (x), crosswind (y) and vertical (z) directions respectively, was simulated with a grid resolution of $nx \times ny \times nz = 1024 \times 384 \times 256$. Here nx, ny, nz are the number of grid nodes in along wind, crosswind and vertical directions, respectively. This implies that the size of a grid cell is $0.98^3 \, \text{m}^3 \approx 1 \, \text{m}^3$. The release points were located at 25 m and 150 m above the ground. A total of 100 time frames were calculated with a time resolution of 1.5625 s. We used the Parallelized Large-Eddy Simulation Model (PALM, Raasch and Schröter, 2001; Maronga et al., 2015) to solve the filtered, incompressible Navier-Stokes equations in Boussinesq-approximated form, at infinite Reynolds number. For further information on the model set-up see Ardeshiri et al. (2019).

WHAT IS THE WIND SPEED?

2.2 Radiative transfer simulations

The 3D MYSTIC Monte Carlo radiative transfer model was used to calculate UV camera images (Mayer et al., 2010; Emde et al., 2010; Buras and Mayer, 2011; Kylling et al., 2020). To simulate a camera with a prescribed number of pixels, MYSTIC was run in backward mode and calculated the radiation impinging the camera plane defined by the location of the camera within a 3D domain and the camera viewing direction. Camera images were calculated for wavelengths suitable for the detection of SO$_2$. For each camera pixel, spectra were calculated for wavelengths between 300 and 350.5 nm with a spectral resolution of 0.1 nm in order to capture the fine structure of the SO$_2$ cross section. The spectra were weighted with spectral response functions (about 10 nm width) representing cameras with mounted on-band (sensitive to SO$_2$ absorption, centred at 310 nm) and off-band (barely sensitive to SO$_2$ absorption, centred about 330 nm) filters similar to those described by Gliß et al. (2018). Quantum efficiency of the detector and geometrical effects related to lens/camera optics are not included in the camera simulations. SO$_2$ plume concentrations were taken from the LES simulations and the spectrally dependent SO$_2$ absorption cross section was from Hermans et al. (2009). For representing the ambient atmosphere the mid-latitude summer atmosphere of Anderson et al. (1986) was used. The surface albedo is small in the UV for non-snow covered surfaces and was thus set to zero. Aerosols were not included. The solar zenith angle was $40°$ and the sun azimuth angle was perpendicular to the camera viewing direction, see Fig. 1.

As in Kylling et al. (2020) cameras at four different locations were simulated. Their location and viewing geometries are summarized in Table 1 and a bird's eye view is shown in Fig. 1. Camera A views the plume from its release point and about 200 m downwind. For camera A the plume release altitude was 25 m and the camera A thus have low angle viewing elevations, see Table 1. For cameras B, C and D the plume release altitude was 150 m and these cameras thus have a larger viewing elevation. Camera A is placed at the same x-direction location as camera A, but as a smaller horizontal FOV to focus on the more mature parts of the plume. Cameras C and D are placed further downwind and views more dispersed parts of the plume about 300 and 500 m downwind from the release point, respectively.

Table 1. Location and geometric specification of the four simulated cameras. All cameras were placed 1 meter above the surface. Adopted from Kylling et al. (2020).

Camera	FOV (degrees)	Viewing elevation (degrees)	No. of pixels. (horizontal×vertical)	x-location (m)
A	46°×10°	5.73°	400×88	500
B	11.5°×30°	30.7°	100×264	500
C	11.5°×30°	30.7°	100×264	700
D	11.5°×30°	30.7°	100×264	900
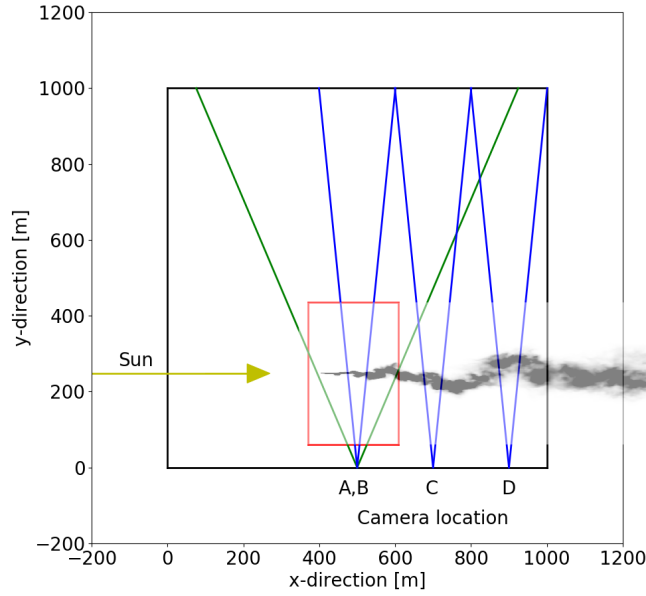
Figure 1. Bird's eyes view of the 3D domain (black square) and the SO$_2$ plume location within the camera A domain simualtion (red square). The UV camera is located where the two green or blue lines intersect. The lines indicate the cameras' horizontal field-of-view. The direction of the incoming sun ray is indicated by the yellow line. The plume column density is included for illustrative purposes. Adopted from Kylling et al. (2020).

From the on and off-band radiances, $I_{on,\,off,M}$, the apparent absorbance was calculated (Mori and Burton, 2006; Lübcke et al., 2013)

$$\tau = \tau_{on} - \tau_{off} = -\ln\frac{I_{on,M}}{I_{on,0}} + \ln\frac{I_{off,M}}{I_{off,0}} = \ln\left(\frac{I_{off,M}}{I_{on,M}}\frac{I_{on,0}}{I_{off,0}}\right), \tag{1}$$

4

where $I_{on,off,0}$ are the background radiances without the SO_2 plume. The background images were calculated similar to the plume images, but with the SO_2 concentration set to zero.

The LES voxel resolution is about 1 m^3 which at a distance of 250 m (roughly distance between cameras and plume) corresponds to 0.004 rad=0.23°. The number of pixels in the simulated images were set to oversample the spatial resolution of the LES simulations by about a factor of two. The number of simulated pixels are smaller than found in real cameras; for example Dinger et al. (2018) used cameras with 1392×1040 pixels and a field of view (FOV) of 14.7°×11.1°. The memory and computer time requirements increase with the numberof pixels, making simulations for so many pixels not currently feasible. Furthermore, the LES input would need to be at higher spatial resolution to justify simulation of cameras with more pixels.

The radiative transfer simulations were run on a Linux cluster utilizing 10 processors in parallel with each process needing about 10 GB of memory. For each pixel and wavelength 2000 photons were traced to ensure that the statistical noise of the MYSTIC Monte Carlo simulations were about the same order of magnitude as the measurements ($\approx$ 1%).

2.3 Velocity analysis

Describe PCS lines

2.3.1 Velocity from optical flow

Describe how it is calculated. Mention that plume flow direction is also derived.

2.3.2 Velocity from cross correlation

Describe how it is calculated

3 Results

3.1 Velocity analysis: synthetic data

In Fig. 2 is shown apparent absorbances for the eight time steps used for the velocity analysis of camera A images. The lines labelled M shows the PCS line used for the cross correlation velocity estimate. The lines labelled L and R are the left and right boundaries of a rectangular box encompassing the region used for the optical flow velocity analysis. In Fig. 2 the PCS line is at x pixel 250. Below, velocity results are presented with the M-line at 100, 150, 200, 250, 300 and 350.

In Fig. 3 is shown the apparent absorption images from cameras at locations B (top row), C (middle row) and D (bottom row). A total of ten time steps were used for these cameras and the M-line was located at 10, 20, 30, 40, 50, 60 and 70.

The velocities at different PCS lines using the cross correlation and optical flow methods are shown for camera A in Fig. 4 and cameras B, C and D in Fig. 5. Also shown in Figs. 4 and 5 are the plume directions as derived from the optical flow.
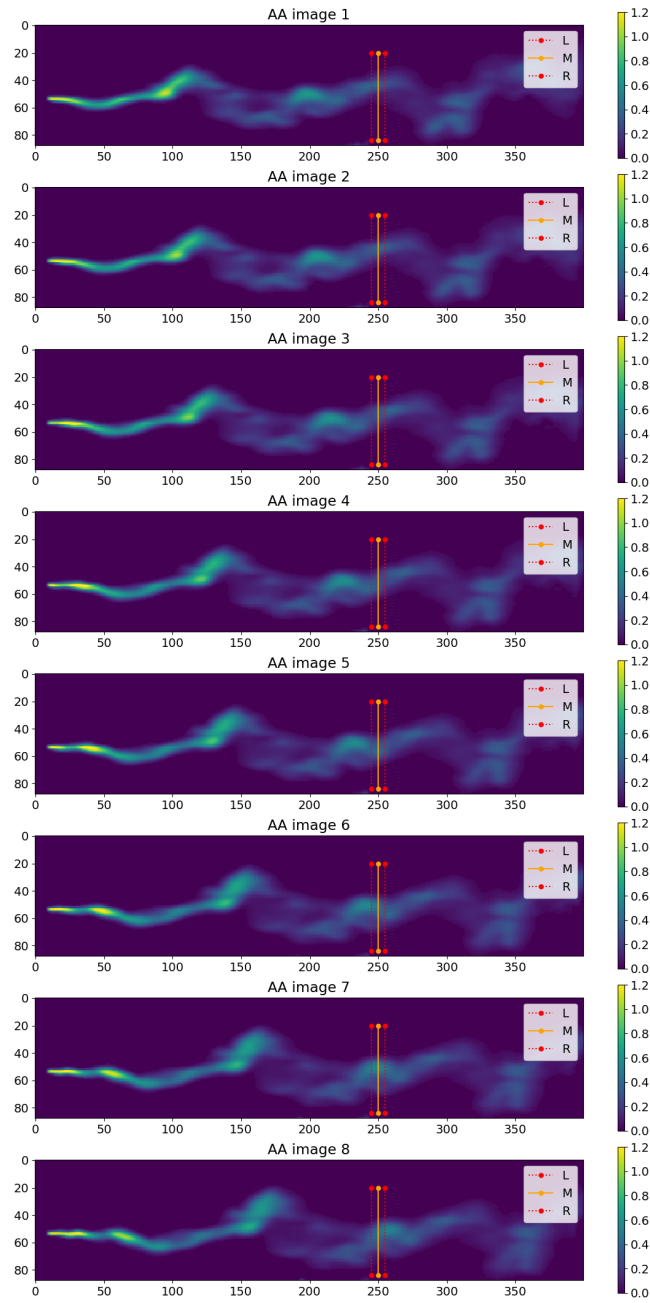
Some velocities missing because:

Figure 2. The apparent absorbance as derived from camera A images. The lines labelled M shows the PCS line used for the cross correlation velocity estimate. The lines labelled L and R are the left and right boundaries of a rectangular box encompassing the region used for the optical flow velocity analysis. Units on x- and y-axes are in pixels.
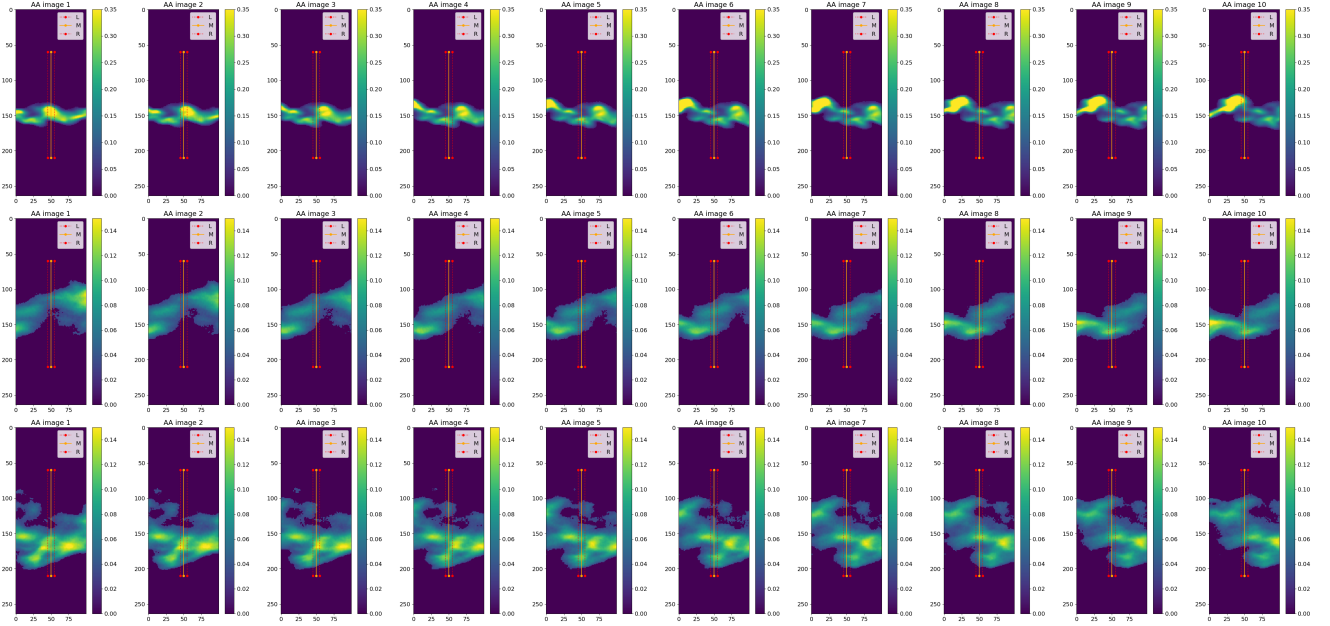
Figure 3. Apparent absorption (AA) images from cameras at locations B (top row), C (middle row) and D (bottom row) and time steps 1 to 10 (columns 1 to 10). PCS lines similar as in Fig. 2. Note different scales on colorbars.

```
plumespeed.py(l3088,local_flow_params()): Aborting histogram analysis:
Multi-Gauss fit yielded additional Gaussian exceeding significance
thresh of 0.2 in histo of orientation angles

Significance: 30.67963866968083 %
Significance: 31.873164606888327 %
Significance: 23.06423881656792 %
Significance: 35.02810714760371 %
Significance: 61.6043930700684 %
Significance: 28.69744270222855 %
Significance: 59.029779606658074 %
Significance: 30.697942504522068 %
Significance: 21.73517476305695 %

Limit hard-coded to 0.2 in plumespeed.py
```
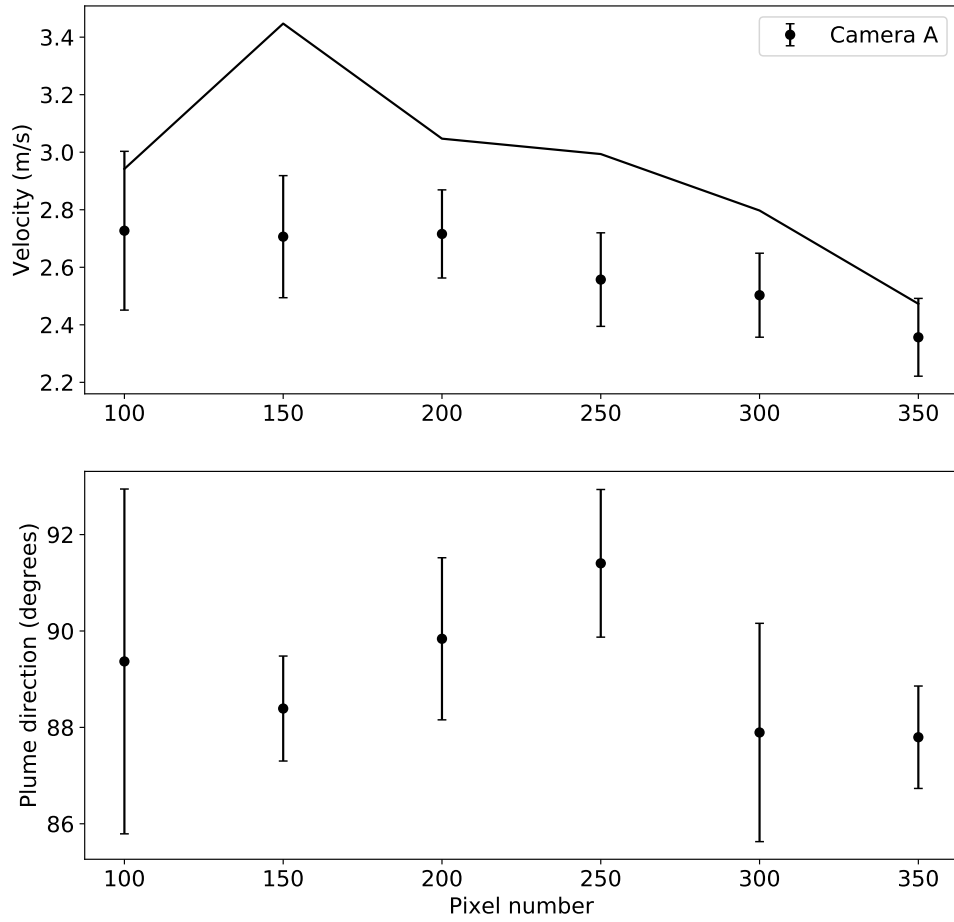
Figure 4. (Top) The average plume velocity as determined by the optical flow method (dots) where error bars indicate the standard deviation. The velocity is determined at a plume cross section at the pixel given at the x-axis. The solid line is the plume velocity determined using cross correlation analysis. (Bottom) The average plume direction and standard deviation indicated by error bars. Determined with the optical flow analysis.

3.2 Velocity analysis: measured data

Use continuous release data from Rena and/or data from Stromboli

8
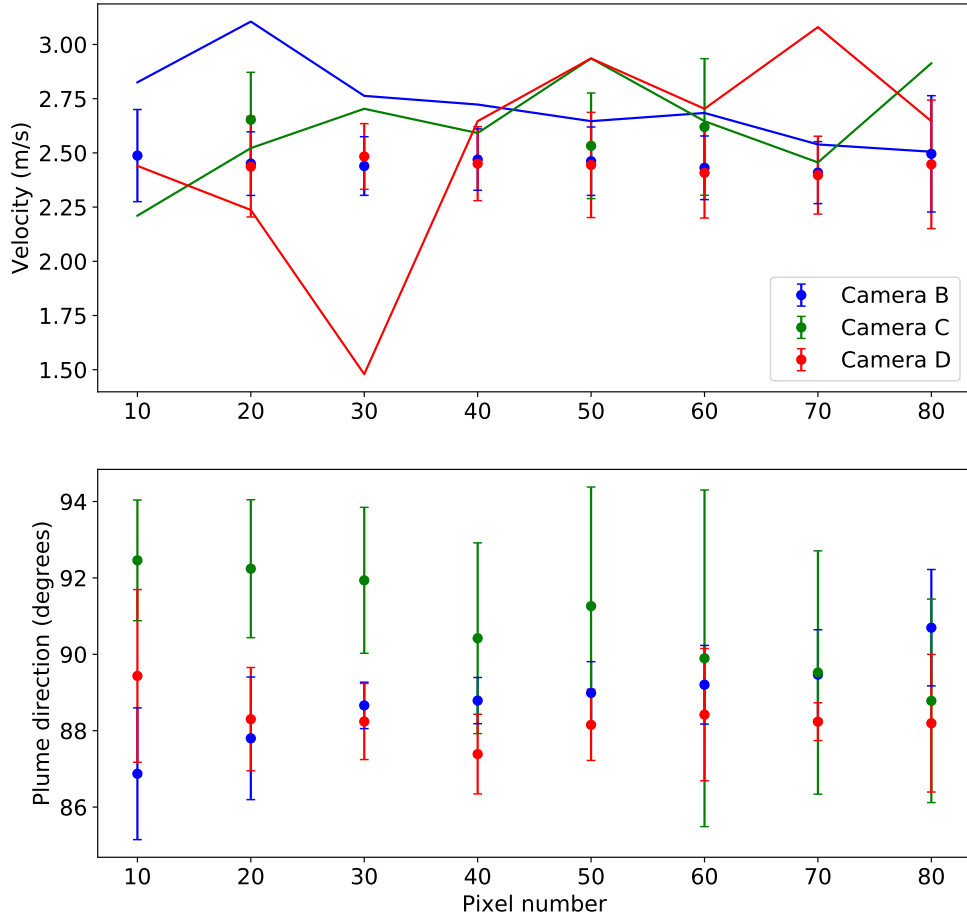
Figure 5. Similar to Fig. 4, but for cameras B, C and D.

4 Conclusions

5 References

Anderson, G., Clough, S., Kneizys, F., Chetwynd, J., and Shettle, E.: AFGL atmospheric constituent profiles (0-120 km), *Tech. Rep. AFGL-TR-86-0110*, Air Force Geophys. Lab., Hanscom Air Force Base, Bedford, Mass., 1986.

Ardeshiri, H., Park, S. Y., Cassiani, M., Stohl, A., Stebel, K., Pisso, I., and Dinger, A. S.: Effects of grid resolution on large eddy simulation of plume dispersion in an infinite-Re neutral boundary layer, Submitted to Journal of Fluid Mechanics, 2019.

Buras, R. and Mayer, B.: Efficient unbiased variance reduction techniques for Monte Carlo simulations of radiative transfer in cloudy atmospheres: The solution, J. Quant. Spectrosc. Radiat. Transfer, 112, 434–447, doi:10.1016/j.jqsrt.2010.10.005, 2011.

Celik, I., Klein, M., and Janicka, J.: Assessment measures for engineering les application, J. Fluid Eng, 131(3), 031 102, 2009.

Deardorff, J.: The use of subgrid transport equations in a three-dimensional model of atmospheric turbulence, J. Fluid Eng, 95, 429–438, 1973.

Dinger, A. S., Stebel, K., Cassiani, M., Ardeshiri, H., Bernardo, C., Kylling, A., Park, S.-Y., Pisso, I., Schmidbauer, N., Wasseng, J., and Stohl, A.: Observation of turbulent dispersion of artificially released SO_2 puffs with UV cameras, Atmospheric Measurement Techniques, 11, 6169–6188, https://doi.org/10.5194/amt-11-6169-2018, https://www.atmos-meas-tech.net/11/6169/2018/, 2018.

Emde, C., Buras, R., Mayer, B., and Blumthaler, M.: The impact of aerosols on polarized sky radiance: model development, validation, and applications, Atmos. Chem. Phys., 10, 383–396, http://www.atmos-chem-phys.net/10/383/2010/, 2010.

Emde, C., Buras-Schnell, R., Kylling, A., Mayer, B., Gasteiger, J., Hamann, U., Kylling, J., Richter, B., Pause, C., Dowling, T., and Bugliaro, L.: The libRadtran software package for radiative transfer calculations (version 2.0.1), Geoscientific Model Development, 9, 1647–1672, https://doi.org/10.5194/gmd-9-1647-2016, http://www.geosci-model-dev.net/9/1647/2016/, 2016.

Gliß, J., Stebel, K., Kylling, A., and Sudbø, A.: Improved optical flow velocity analysis in SO_2 camera images of volcanic plumes – implications for emission-rate retrievals investigated at Mt Etna, Italy and Guallatiri, Chile, Atmospheric Measurement Techniques, 11, 781–801, https://doi.org/10.5194/amt-11-781-2018, https://www.atmos-meas-tech.net/11/781/2018/, 2018.

Hermans, C., Vandaele, A., and Fally, S.: Fourier transform measurements of SO_2 absorption cross sections:: I. Temperature dependence in the 24 000-29 000 cm^{-1} (345-420 nm) region, Journal of Quantitative Spectroscopy and Radiative Transfer, 110, 756–765, https://doi.org/http://dx.doi.org/10.1016/j.jqsrt.2009.01.031, http://www.sciencedirect.com/science/article/pii/S0022407309000375, {HITRAN}, 2009.

Kylling, A., Buras, R., Eckhardt, S., Emde, C., Mayer, B., and Stohl, A.: Simulation of SEVIRI infrared channels: a case study from the Eyjafjallajökull April/May 2010 eruption, Atmospheric Measurement Techniques, 6, 649–660, https://doi.org/10.5194/amt-6-649-2013, http://www.atmos-meas-tech.net/6/649/2013/, 2013.

Kylling, A., Ardeshiri, H., Cassiani, M., Dinger, A. S., Park, S.-Y., Pisso, I., Schmidbauer, N., Stebel, K., and Stohl, A.: Can statistics of turbulent tracer dispersion be inferred from camera observations of SO_2 in the ultraviolet? A modelling study, Atmospheric Measurement Techniques, 13, 3303–3318, https://doi.org/10.5194/amt-13-3303-2020, https://amt.copernicus.org/articles/13/3303/2020/, 2020.

Lübcke, P., Bobrowski, N., Illing, S., Kern, C., Alvarez Nieves, J. M., Vogel, L., Zielcke, J., Delgado Granados, H., and Platt, U.: On the absolute calibration of SO_2 cameras, Atmospheric Measurement Techniques, 6, 677–696, https://doi.org/10.5194/amt-6-677-2013, http://www.atmos-meas-tech.net/6/677/2013/, 2013.

Maronga, B., Gryschka, M., Heinze, R., Hoffmann, F., Kanani-Sühring, F., Keck, M., Ketelsen, K., Letzel, M. O., Sühring, M., and Raasch, S.: The Parallelized Large-Eddy Simulation Model (PALM) version 4.0 for atmospheric and oceanic flows: model formulation, recent

developments, and future perspectives, Geoscientific Model Development, 8, 2515–2551, https://doi.org/10.5194/gmd-8-2515-2015, https://www.geosci-model-dev.net/8/2515/2015/, 2015.

Mayer, B. and Kylling, A.: Technical note: the libRadtran software package for radiative transfer calculations-description and examples of use, Atmos. Chem. Phys., 5, 1855–1877, 2005.

Mayer, B., Hoch, S. W., and Whiteman, C. D.: Validating the MYSTIC three-dimensional radiative transfer model with observations from the complex topography of Arizona's Meteor Crater, Atmos. Chem. Phys., 10, 8685–8696, 2010.

Moeng, C.: A large-eddy simulation model for the study of planetary boundary-layer turbulence, J. Atmos. Sci, 41, 2052–2062, 1984.

Mori, T. and Burton, M.: The SO2 camera: A simple, fast and cheap method for ground-based imaging of SO2 in volcanic plumes, Geophysical Research Letters, 33, https://doi.org/10.1029/2006GL027916, https://agupubs.onlinelibrary.wiley.com/doi/abs/10.1029/2006GL027916, 2006.

Pope, S. B.: Turbulent Flows, Cambridge University Press, 2000.

Raasch, S. and Schröter, M.: PALM A large-eddy simulation model performing on massively parallel computers, Meteorologische Zeitschrift, 10, 363–372, https://doi.org/doi:10.1127/0941-2948/2001/0010-0363, https://www.ingentaconnect.com/content/schweiz/mz/2001/00000010/00000005/art00001, 2001.